Published in final edited form as:
Clin Cancer Res. 2014 December 15; 20(24): 6367–6378. doi:10.1158/1078-0432.CCR-14-1452.

Applications of immunoPET: using ^{124}I-anti-PSCA A11 minibody for imaging disease progression and response to therapy in mouse xenograft models of prostate cancer

Scott M. Knowles[1], **Richard Tavaré**[1], **Kirstin A. Zettlitz**[1], **Matthew M. Rochefort**[2], **Felix B. Salazar**[1], **Ziyue Karen Jiang**[1,3], **Robert E. Reiter**[3], and **Anna M. Wu**[1]

[1]Crump Institute for Molecular Imaging, Department of Molecular and Medical Pharmacology, David Geffen School of Medicine at the University of California-Los Angeles

[2]Department of Surgery, David Geffen School of Medicine at the University of California-Los Angeles

[3]Department of Urology, David Geffen School of Medicine at the University of California-Los Angeles

Abstract

Purpose—Prostate stem cell antigen (PSCA) is highly expressed in local prostate cancers and prostate cancer bone metastases and its expression correlates with androgen receptor activation and a poor prognosis. In this study, we investigate the potential clinical applications of immunoPET with the anti-PSCA A11 minibody, an antibody fragment optimized for use as an imaging agent. We compare A11 minibody immunoPET to ^{18}F-Fluoride PET bone scans for detecting prostate cancer bone tumors and evaluate the ability of the A11 minibody to image tumor response to androgen deprivation.

Experimental Design—Osteoblastic, PSCA expressing, LAPC-9 intratibial xenografts were imaged with serial ^{124}I-anti-PSCA A11 minibody immunoPET and ^{18}F-Fluoride bone scans. Mice bearing LAPC-9 subcutaneous xenografts were treated with either vehicle or MDV-3100 and imaged with A11 minibody immunoPET/CT scans pre- and post-treatment. *Ex vivo* flow cytometry measured the change in PSCA expression in response to androgen deprivation.

Results—A11 minibody demonstrated improved sensitivity and specificity over ^{18}F-Fluoride bone scans for detecting LAPC-9 intratibial xenografts at all time points. LAPC-9 subcutaneous xenografts showed downregulation of PSCA when treated with MDV-3100 which A11 minibody immunoPET was able to detect *in vivo*.

Corresponding Author: Anna M. Wu, 570 Westwood Plaza, Box 951770, Los Angeles, CA 90095-1770, (T) 310-794-5088 (F) 310-206-8975, awu@mednet.ucla.edu.
First Author: Scott M. Knowles, (T) 310-267-2819, sknowles@mednet.ucla.edu

Disclosures:

Scott M. Knowles, Richard Tavaré, Kirstin A. Zettlitz, Matthew M. Rochefort, Felix B. Salazar, and Ziyue Karen Jiang have no relevant or material financial interests or other conflicts or interest.

Robert E. Reiter and Anna M. Wu are shareholders and consultants of ImaginAb Inc. which has licensed some of the technology described in this manuscript.

Conclusions—A11 minibody immunoPET has the potential to improve the sensitivity and specificity of clinical prostate cancer metastasis detection over bone scans, which are the current clinical standard of care. A11 minibody immunoPET additionally has the potential to image the activity of the androgen signaling axis *in vivo* which may help evaluate the clinical response to androgen deprivation and the development of castration resistance.

Keywords

immunoPET; minibody; Prostate Stem Cell Antigen (PSCA); prostate cancer bone metastases; MDV-3100 (enzalutamide)

Introduction

There is a significant clinical need for improving the detection of prostate cancer metastases and measuring the response of tumors to systemic therapy. The most common method of screening for prostate cancer, a prostate specific antigen (PSA) blood test, is notoriously non-specific and is commonly elevated in benign prostate hyperplasia (BPH), prostatitis, and low-risk indolent prostate cancer. Prostate cancer survival is high for the 91% of patients that are diagnosed with local or regional disease and PSA testing is associated with over-diagnosis and treatment of indolent disease (1). On the other hand, prostate cancer is the second most common cause of cancer related deaths in men and one of the great challenges in treating it is distinguishing the patients who do not need to be treated from those for whom it is life threatening (2). Metastases, and especially bone metastases, represent the primary cause of morbidity and mortality and prostate cancer survival rates fall quickly once the disease has metastasized to distant sites (2). Detection of metastases, therefore, stratifies a subset of patients that need to be treated aggressively and systemically from the large majority of patients where more conservative local therapies or active surveillance is preferred. Following the detection of distant metastases, androgen deprivation becomes the standard of care and PSA tests are frequently used to monitor the effectiveness of androgen deprivation and the development of castration resistant prostate cancer (CRPC). However, PSA levels can only measure the response of the tumors as a whole and cannot determine whether there is an androgen independent subset of tumors that fails to respond and may necessitate the use of targeted radiation or chemotherapy. There is a need for an imaging modality that can improve the early detection and localization of prostate cancer metastases and image response to androgen deprivation therapy in order to guide therapeutic decision-making.

Despite the large influence of bone metastases on patient prognosis and therapy decisions, the current methods of detecting them are unsatisfactory. Most current clinical monitoring for metastases utilizes ^{99m}Tc-Methylene diphosphonate (^{99m}Tc-MDP) planar or SPECT imaging of bone formation in response to osteoblastic prostate cancer bone metastases, though other methods are at various stages of development (3, 4). Bone scans are clinically recommended for symptomatic patients and asymptomatic men with serum PSA >10–20ng/mL, however, due to relatively low sensitivity of bone scans and their inability to detect metastases to other sites the presence of prostate cancer recurrence and/or metastasis

often must be inferred based on other risk factors such as a rising PSA in a patient who has received a radical prostatectomy (4).

Recently ^{18}F-Fluoride PET bone scans have shown improved sensitivity over ^{99m}Tc-MDP in initial small clinical trials and are currently the subject of a Phase III study to determine whether their use improves metastasis detection (5–8). However, while the sensitivity of bone metastasis detection may be improved using ^{18}F-Fluoride bone scans, bone scans are obviously limited to detecting metastases to bone without the ability to image local prostate cancer or metastases to other sites. Bone scans also have considerable false positives due to any benign process that increases bone formation such as trauma and fractures, degenerative diseases (e.g. osteoporosis), Paget's disease, and inflammatory processes (e.g. arthritis) which are relatively common in the elderly patients most likely to develop prostate cancer (4, 8). Bone scans, additionally, have difficulty measuring response to therapy due to the flare phenomenon where uptake in bone scan lesions often increases in response to therapy due to bone healing in response to the shrinking tumor. This flare can last for months after successful therapy has been initiated and lesions may continue to appear on bone scans long after the viable tumor has been eliminated (4).

While the mainstay of metastatic prostate cancer therapy is androgen deprivation therapy (ADT), patients progress to CRPC a median of 2–3 years after initiating treatment (9). MDV-3100 (enzalutamide) is a second-generation anti-androgen that has recently won FDA approval for the treatment of CRPC (10). MDV-3100 has continued efficacy in cell lines resistant to other anti-androgens and results in a larger repression of androgen dependent genes and shorter time period to maximal efficacy than castration in mouse models (11–13). A phase III study of MDV-3100 showed a ≥50% PSA decrease in 54% of patients who had previously failed both ADT and chemotherapy regimens and prolonged median survival 4.8 months over placebo (14). However, many patients do not respond to therapy with MDV-3100 and many initial responders develop resistance rapidly possibly through the generation of constitutively active splice variants that lack the AR C-terminal ligand binding domain on which MDV-3100 acts (15–17). A method of imaging the activity of the androgen receptor signaling axis *in vivo* could lead to improved therapeutic strategies and could allow for targeted radiation therapy or a more prompt transition to alternative androgen deprivation agents or systemic chemotherapy in the patients whose tumors reactivate the androgen-signaling axis.

Prostate stem cell antigen (PSCA) is highly expressed in 83–100% of prostate cancers and overexpressed in the great majority of prostate cancer bone metastases (87–100%) and in many metastases to other sites (67% liver, 67–95% lymph node) (18–21). Its expression correlates with the Gleason score, tumor invasion, androgen independence, metastasis, and a poor prognosis (21–26). The PSCA promoter contains an androgen response element and PSCA expression is regulated by androgens in the normal mouse prostate (27, 28). Likewise, androgen deprivation decreases PSCA mRNA expression in human high-grade prostatic intraepithelial neoplasia (HGPIN) and prostate cancer (29, 30). We have previously shown that immunoPET with an affinity matured ^{124}I-labeled A11 anti-PSCA minibody, an antibody fragment with pharmacokinetics optimized for imaging, can be used for specific and quantitative imaging of PSCA expression *in vivo* (31–33). We therefore hypothesize that

imaging PSCA expression using the A11 minibody may outperform bone scans for imaging prostate cancer bone metastases and allow for imaging changes in PSCA expression in response to androgen deprivation. In this work, we will compare the sensitivity of the A11 minibody to ^{18}F-Fluoride bone scans for detecting bone tumors using a naturally PSCA expressing, purely osteoblastic, LAPC-9 intratibial xenograft model. We will also investigate changes in PSCA expression in LAPC-9 subcutaneous xenografts in response to androgen deprivation with MDV-3100 and demonstrate that anti-PSCA A11 minibody immunoPET can image these changes *in vivo*.

Materials and Methods

Subcutaneous and intratibial xenograft models

LAPC-9 subcutaneous (s.c.) xenografts were passaged surgically in male SCID mice as previously described (34). Single cell suspensions of LAPC-9 cells were prepared by digesting freshly excised LAPC-9 s.c. xenografts in 0.1% Pronase (Sigma) in Iscove's Modified Dulbecco's Medium (IMDM, Gibco) for 18 minutes at room temperature (35, 36). The cells were then passaged through 18 gauge needles and strained through a 70μm cell strainer (BD Biosciences). 1 ×10^5 viable cells were prepared in 10μL of 1:1 Media:Matrigel and injected into the tibias of anesthetized male SCID mice by drilling a needle through the proximal end of the tibial plateau. Once the needle tip entered the intramedullary space of the tibial metaphysis, the cells were slowly injected and the needle was removed (37). A sham injection, where the needle was inserted using the same method, but only Media:Matrigel was injected, was performed on the contralateral leg. Injections of PSCA-Negative 22rv1 cells and 22rv1 ×PSCA cells transfected with PSCA were used respectively as negative and positive controls (see supplemental materials). All animal experiments were conducted in compliance with a protocol approved by the Institutional Animal Care and Use Committee of the University of California-Los Angeles.

^{18}F-Fluoride and A11 minibody imaging of intratibial xenografts

Intratibial tumor bearing mice were serially imaged with both bone scans and immunoPET at 4, 6, and/or 8 weeks post-intratibial injection. Intratibial xenograft bearing mice were injected with ~100μCi of ^{18}F-Fluoride in 100μL of saline via tail vein injection. After an hour of conscious uptake, the mice were anesthetized, their bladders were manually expressed, and the mice were imaged with a 10 minute acquisition on an Inveon microPET scanner (Siemens Preclinical Solutions) followed by a microCT scan (MicroCAT II, Siemens Preclinical Solutions). MicroPET and microCT were automatically co-registered based on empirically determined scanner alignments. All image manipulation and quantification was performed using AMIDE (38). Alignment was manually verified and adjusted using the bladder as a fiduciary marker. Uptake (%ID/g) was then quantified from the co-registered microPET/CT images using microCT isocontour ROIs (≥200 Hounsfield units) to capture a region encompassing either only the tumor bearing tibia or the sham tibia. The mean value of the microPET scan was converted to %ID/g using the decay corrected injected dose of ^{18}F-Fluoride and an empirically determined cylinder factor for ^{18}F.

Either immediately following the ^{18}F-Fluoride bone scan or the day following the bone scan the intratibial tumor bearing mice were injected with ~3μg ^{124}I-labeled A11 minibody. Radiolabeling, purification, and immunoreactivity were performed as previously described except for the much higher specific activity used here (~30–50μCi/μg) (32). 44 hours after A11 minibody injection, the mice again received microPET/CT scans. The mice were then either kept for serial imaging at later time points or at the last time point sacrificed for biodistribution as previously described (32). The images were analyzed using the same method as for the ^{18}F-Fluoride bone scans. No partial volume correction was performed on either the ^{18}F-Fluoride or ^{124}I-A11 immunoPET as determining the tumor volume by CT would be too arbitrary to be reproducible and hence only quantification of the entire tibia was performed without attempting to approximate the tumor boundaries. This method provided the additional benefit of allowing direct comparison between the biodistribution and imaging results.

High resolution *ex vivo* microCT and histology

Following biodistribution, tibias were stored in 10% phosphate buffered formalin until radioactivity had decayed. The tibias were then analyzed *ex vivo* by 20μm resolution microCT (μCT40, SANCO Medical). Volume renderings were generated with OsirX 5.6 (39). The tibia samples were then decalcified and embedded in paraffin and sectioned for histological analysis. Only those mice with intratibial tumor establishment confirmed by gross and/or histological analysis were included in the analysis.

A11 minibody imaging of response to therapy with MDV-3100

LAPC-9 s.c. xenografts were implanted bilaterally and allowed to grow for 3 weeks. The mice then received a pre-treatment A11 minibody immunoPET/CT at 44 hours post-injection as previously described, with the exception that each mouse received a dose of ~50μg of ^{124}I-A11 minibody (32). Immediately following the pre-treatment scan the mice were randomized into treatment groups and received either 40mg/kg MDV-3100 (ChemScene) or vehicle by daily gavage. The vehicle consisted of 300μL of water with 1% carboxymethylcellulose (Sigma-Aldrich), 0.1% Tween-80 (Sigma-Aldrich) and 1.6% DMSO. After five days of treatment, one mouse from each group underwent a microPET/CT scan to confirm that minimal signal was retained from the first imaging injection, and then all mice were again injected with ~50μg of ^{124}I-labeled A11 minibody. On the 7th day of treatment, 44 hours post-A11 minibody injection, the mice received a post-treatment scan following which the mice were sacrificed and biodistribution and microPET image analysis and quantification with partial volume correction were performed as previously described (32). The tumors were then fixed and examined histologically (see supplemental materials).

Quantitative flow cytometry

LAPC-9 s.c. xenograft bearing mice treated identically to the imaging cohorts, except without the injection of the radioactive tracers, were used for quantitative flow cytometry. Following 7 days of treatment with MDV-3100 or vehicle, mice were sacrificed and LAPC-9 tumors were reduced to single cell suspensions by incubation in 1mg/mL

collagenase IV (Sigma) in HBSS for 1 hour at 37°C. The cells were then passaged through 18 and 24 gauge needles followed by a 70μM cell strainer (BD Biosciences). 5×10^5 LAPC-9 cells from each tumor were incubated in 16μg/mL (~100nM) 1G8 mouse anti-PSCA antibody (produced as previously described) followed by 8μg/mL (~50nM) Dylight-649 conjugated anti-mouse-Fc_γ secondary antibody (Jackson ImmunoResearch) (40). Following secondary antibody incubation, samples were incubated with Alexa-488 anti-PSMA antibody (FOLH1, BioLegend) and stained with 7-AAD (BD Biosciences), as per the manufacturers' instructions, to allow gating for viable prostate epithelial cells. The final analyzed population was FSC and SSC gated, 7-AAD^{Low}, $PSMA^+$. Acquisition was performed with an LSRII flow cytometer (BD) and analysis was performed in FlowJo 9.3.2 (TreeStar). PSCA receptor density was quantified using the QIFIKIT calibration beads (Dako) as per the manufacturer's instructions.

Data analysis

Statistical analysis of both the bone scans and the immunoPET scans in the intratibial model were performed using two-way repeated measure ANOVA with intra-time-point significance testing and adjustments for multiple comparisons performed using the Holm-Šidák method. As the variance of the A11 immunoPET dataset increases significantly as the uptake increases, a log-transformation was applied to fulfill the homoscedasticity requirement of both ANOVA and Holm-Šidák before significance testing. Significance testing of the MDV-3100 response to therapy model was performed using two-tailed Student's t-tests. The 95% confidence level ($p<0.05$) was used for all analysis. Except where indicated otherwise all values are reported as mean±SD. All microPET images are displayed as full thickness maximum intensity projections.

Results

Radiolabeling

^{124}I-labeled A11 minibody used in the intratibial xenograft model had a mean specific activity of 23.7±6.5μCi/μg (n=8). After purification by size exclusion, the mean purity of the protein injected was 95±5% with immunoreactivity of 62±5%. For the MDV-3100 treatment model, the specific activity for the pre-treatment imaging was 1.23μCi/μg with injected radiochemical purity of 93.8% and immunoreactivity of 72.7%. The post-treatment imaging had specific activity of 2.38μCi/μg, radiochemical purity of 98.6%, and immunoreactivity of 83.3%.

Comparison of ^{18}F-Fluoride ion bone scans and ^{124}I-A11 minibody immunoPET in mice bearing intratibial xenografts

^{18}F-Fluoride bone scans of mice bearing LAPC-9 intratibial xenografts show a large amount of non-specific uptake and a qualitative increase in the positive tibia over the negative tibia in only 16.7% of mice at 4 weeks (1/6), 50% (3/6) at 6 weeks, and 50% (1/2) at 8 weeks (Figure 1A). Quantification of the ^{18}F-Fluoride bone scans shows an overall increase in tibial uptake of ^{18}F-Fluoride in the tumor bearing tibia for all time points in aggregate ($p=0.01$, two-way ANOVA), with no trend in increased uptake in the positive tibia over time ($p=0.89$). The negative tibias show a large amount of non-specific background uptake,

especially in the knee, which leads to a large degree of overlap between the positive and negative tibias and makes quantitative determination of a positive signal due to tumor growth difficult. In fact, the increase in ^{18}F-Fluoride uptake in the positive tibia only reaches significance in aggregate across time points and fails to reach significance for any individual time point on its own (Figure 1B).

A11 minibody immunoPET imaging shows intratibial tumor targeting which can be appreciated above blood activity in 67% of mice (4/6) at 4 weeks, 100% of mice (6/6) at 6 weeks and 100% of mice at 8 weeks (2/2) post-xenograft implantation (Figure 2A). Imaging of two mice at 8 weeks post-intratibial tumor implantation shows that the tumor has invaded through the bone and into the surrounding muscle. Quantification of the serial A11 immunoPET scans shows an overall increase in tibial uptake of the A11 minibody in the tumor bearing tibia across all time points ($p<0.0001$, two-way ANOVA), with an increase in the positive tibia over time ($p=0.001$). Due to the high specificity of the A11 minibody and universally low background in normal bone, the positive tibia has significantly higher uptake at all time points (Figure 2B). The high specificity of A11 minibody, therefore, allows for highly sensitive imaging of bone tumors as any bone uptake above blood can be interpreted as a PSCA expressing tumor.

Biodistribution of the LAPC-9 mice at 6 (n=4) or 8 weeks (n=2) post-tumor-implantation confirms the results of the immunoPET imaging (Table 1). The 6 week post-implantation mice show an average of 1.51±0.79%ID/g uptake in the positive tibia and 0.08±0.03%ID/g in the negative tibia ($p=0.02$). At 8 weeks post-injection the uptake is similar with 1.50±0.35%ID/g in the positive tibia and 0.12±0.00%ID/g in the negative tibia.

A11 minibody immunoPET of mice bearing negative control 22rv1 intratibial tumors (n=5) showed no distinguishable intratibial uptake by microPET and showed only a small increase in tibial uptake (0.36±0.19%ID/g) compared to the contralateral sham tibia (0.08±0.02%ID/g) by biodistribution ($p=0.025$). The small increase in intratibial uptake in the 22rv1 tumor was less than the blood activity (0.40±0.11%ID/g) and was likely a result of the enhanced permeability and retention (EPR) effect uptake due to malformed tumor vasculature. Biodistribution of a mouse bearing a 22rv1 ×PSCA intratibial xenograft at 6 weeks post-injection showed uptake of 3.31%ID/g for the 22rv1 ×PSCA tibia, 46.9 times higher than the sham tibia, 8.5 times higher than tibias bearing 22rv1 tumors, and 10.7 times higher than blood (Supplemental Table 1 and Supplemental Figures 1–4).

Ex vivo microCT and Histology

Gross analysis, *ex vivo* microCT, and histology confirm the presence of an osteoblastic intratibial tumor with spiculated bone formation in each mouse. High resolution *ex vivo* microCT imaging of the LAPC-9 xenograft bearing tibias and the sham controls shows spiculated bone formation in the LAPC-9 bearing tibias with sham injected tibias showing normal appearing bone (Figure 3A). Histology of LAPC-9 bearing tibias shows osteoblastic tumor formation, consistent with previous reports, whereas histology of sham injected tibias shows normal bone marrow (Figure 3B) (35, 36, 41–46). For mice that grew muscle tumors due to missed intratibial injections, neither gross analysis, nor histology, showed the presence of tumor cells in the intramedullary space and on biodistribution only the ipsilateral

muscle uptake of A11 minibody was elevated due to the tumor presence and these mice were excluded from the analysis.

Changes in PSCA expression with MDV-3100 treatment

Quantitative flow cytometry on digested LAPC-9 tumors following 7 days of treatment with MDV-3100 (40mg/kg) or vehicle shows that MDV-3100 treatment downregulates PSCA expression 62.8±4.9% ($p<0.0001$, $n=4$) compared to the vehicle treated control (Figure 4A). Quantitative flow finds expression of 4.75×10^5PSCA antigens per cell for vehicle treated mice whereas mice treated with MDV-3100 express only 1.65×10^5 PSCA antigens per cell.

ImmunoPET imaging of PSCA downregulation in response to androgen deprivation therapy

Partial volume corrected quantification of the pre-treatment results shows equivalent tumor volumes and uptake in the two groups before treatment is initiated (2.43±0.428%ID/g Vehicle, 2.65±0.72%ID/g MDV-3100, $p=0.46$, Figure 4C). After one week of treatment with MDV-3100 tumor volumes show no significant difference as measured by CT ($p=0.54$) or by mass ($p=0.53$). However, following treatment the A11 minibody uptake in the MDV-3100 treated cohort is 29% lower than in the control group by partial volume corrected microPET (3.70±0.20%ID/g Vehicle vs 2.61±0.23%ID/g MDV-3100, $p<0.003$, Figure 4B and Figure 4C) and 24.0% lower than in the vehicle treated controls by biodistribution ($p=0.03$, Table 2).

Normalizing post-treatment imaging by the pre-treatment imaging similarly shows uptake in the MDV-3100 treated group 32% lower than the vehicle treated group ($p=0.0003$). However, rather than the MDV-3100 treated group decreasing from the baseline scan, we find that the MDV-3100 treated group is not significantly changed from pre-treatment (Pre:Post treatment ratio 1.10±0.16, $p=0.90$) and rather the difference post-treatment is due to an increase in the vehicle treated group between the scans (Pre:Post treatment ratio 1.61±0.26, $p=0.0002$).

Discussion

An ideal imaging modality for prostate cancer would allow for early detection of metastases that would inform treatment decisions. Imaging of prostate cancer metastases with an imaging agent specific to the tumor itself instead of imaging a downstream process such as bone formation could yield both higher sensitivity and specificity for detecting prostate cancer bone metastases as well as the potential to image local prostate cancer and metastases to other sites. An ideal imaging modality could likewise determine whether a chosen therapy is effective in a patient. While PSA blood tests can measure the response of the tumors in aggregate, they cannot detect whether only a subset of lesions are resistant to therapy. Molecular imaging of androgen receptor (AR) activity could yield more detailed information regarding individual tumor response to androgen deprivation therapy and development of resistance through the reactivation of AR pathways. ImmunoPET imaging with radiolabeled antibodies targeted to cell surface biomarkers has shown potential for use in this role (13, 31, 47). In previous work, we have shown that ^{124}I-A11 anti-PSCA minibody is capable of

specifically imaging PSCA expressing tumors and that the rapid clearance of the minibody provides excellent imaging contrast at 44 hour post-injection (32, 33). In this work, we demonstrate that A11 minibody immunoPET outperforms the sensitivity and specificity of ^{18}F-Fluoride bone scans for detecting intratibial tumors and can image PSCA downregulation in response the androgen deprivation with MDV-3100 *in vivo*.

While, all LAPC-9 intratibial xenografts in this study show osteoblastic changes and spiculated bone formation on *ex vivo* microCT and histology, bone scans of LAPC-9 intratibial xenografts show qualitative increases over the sham tibia in only 50% (3/6) mice at 6 weeks post-tumor-inoculation indicating that the bone scans missed a significant number of osteoblastic lesions. Even at 8 weeks, when the tumors have eroded through the bone and into the surrounding muscle, the ^{18}F-Fluoride bone scans show only show a fairly subtle and questionable increase in uptake in 50% of mice (1/2). The low sensitivity of the ^{18}F-Fluoride bone scans may have been due to the intratibial tumors' proximity to the non-specific uptake in the tibial growth plate illustrating the problems caused by non-specific uptake of ^{18}F-Fluoride. Quantification of the LAPC-9 bone scans likewise revealed that while there was a significant increase in uptake overall, no significant increase was seen for any time point individually due to the large overlap in uptake between the tumor bearing tibia and the sham control.

Comparison of the bone scans with A11 minibody immunoPET reveals that immunoPET imaging is more sensitive for imaging PSCA expressing bone tumors with 100% (6/6) mice bearing LAPC-9 intratibial xenografts showing clear tumor uptake at 6 weeks. In contrast with the bone scans, A11 minibody immunoPET shows highly specific imaging with minimal activity anywhere in the mouse other than in the PSCA expressing tumor. This high specificity results in easier interpretation of scan results as virtually any lesion above blood activity can be interpreted as a tumor with the exception of only the thyroid, stomach, and bladder due to free ^{124}I released from catabolized antibody. It should be noted that the quantification of the tibial uptake underestimates the actual uptake of A11 minibody in the LAPC-9 tumors by a large margin. While quantification of uptake in the entire tibia was the least biased method of comparing both A11 immunoPET and bone scans and *in vivo* and *ex vivo* measurements using the A11 minibody, the tumor makes up only a fraction of the tibial volume and mass and the %ID/g is decreased by the inclusion of bone and other non-tumor tissue in the measurement.

The results of this work indicate that the A11 minibody has the potential to translate into an imaging agent with higher sensitivity and specificity than bone scans for imaging prostate cancer bone metastases in the clinic. In addition, while bone scans are limited to the detection of relatively large bone metastases that cause osteoblastic changes in the surrounding bone, immunoPET imaging can not only image tumors before changes are seen on bone scan, but also image tumors in locations other than bone. Lymph node metastases, lung metastases, liver metastases, and metastases to other locations have been shown to express PSCA and may be able to be imaged with A11 minibody immunoPET adding to its diagnostic value as up to 19% of patients have been found to have only visceral metastases with no bone involvement (18, 19, 48). In addition, PSCA expression has been correlated

with tumor stage, metastatic potential, and poor outcomes and imaging of PSCA may help stratify patients with high-risk local disease even in the absence of metastases (21–26).

It has previously been suggested that PSCA may be downregulated in prostate cancer in response to androgen deprivation (27–30). In this work, we found that treatment of mice bearing naturally PSCA expressing LAPC-9 xenografts with the anti-androgen MDV-3100 causes a significant, nearly 3-fold, downregulation of PSCA *in vivo*. Imaging of PSCA expression, in addition to helping aid in the localization of metastases, therefore holds the potential for imaging the activity of the AR signaling axis. Following 1 week of treatment, LAPC-9 xenografts treated with MDV-3100 show no significant differences in volume or mass compared to vehicle treated controls. However, the MDV-3100 treated mice show significantly lower uptake of the ^{124}I-A11 minibody than vehicle controls by both microPET and biodistribution. These results suggest that quantitative imaging of PSCA expression holds the potential to measure the efficacy of ADT in men with prostate cancer before changes in tumor volume can be observed. A11 minibody immunoPET may also be effective in imaging the reactivation of the AR axis upon development of CRPC.

Modeling work by Thurber and Weissleder has suggested that antibody uptake into a tumor will only directly reflect antigen expression when the binding sites are relatively close to saturation and that, otherwise, the antibody uptake will be limited by the rate of antibody extravasation from the vasculature and diffusion into the tissue (49). However, large antibody doses and receptor saturation produces a blocking effect that reduces imaging contrast and this effect needs to be balanced with the desire for antigen quantitation. While, the dose of A11 minibody in the response to therapy experiments was increased, the PSCA antigens remained relatively far from saturation and hence the decreased uptake of A11 minibody into the tumor (29%) does not directly reflect the degree of PSCA downregulation (63%). The decrease in A11 minibody uptake with MDV-3100 treatment is significant by both microPET/CT and biodistribution. However, the picture is complicated by comparison to the pre-treatment imaging. Rather than a simple decrease in A11 minibody uptake in the MDV-3100 treated mice compared to the pre-treatment imaging, we instead see an increase in the vehicle treated mice. A11 minibody uptake increased by 59.7±8.5% ($p=0.0002$) in the vehicle treated mice compared to the pre-treatment imaging while the MDV-3100 treated mice show no significant difference between pre- and post-treatment scans ($p=0.90$). These results cannot be explained by differences in Vehicle and MDV-3100 cohort tumor volumes, masses, or necrosis as no significant differences in these variables were observed (Supplemental Figures 5–6). The result was also not due to residual activity from the pre-treatment scan as residual activity was minimal and equivalent between the groups. Other explanations for the increase in uptake post-treatment includes changes in tumor vascularity and permeability as the tumors of both cohorts grew in the 7 days between scans. We recently published a method that uses diffusion-limited kinetic modeling of dynamic imaging with the A11 minibody tumor to measure permeability, vascularity, and antigen concentration independently which we intend to utilize to address these questions in future works (50). Regardless of the cause of the baseline shift between pre- and post-therapy scans, normalizing of post-treatment uptake values by pre-treatment imaging reduces the intra-cohort variance and results in large effect size compared to the non-normalized data

(p=0.0003). While the explanation for the increase in A11 minibody uptake in the vehicle treated group between the pre- and post-treatment scans requires further investigation, there was an unequivocal decrease in uptake in the MDV-3100 treated mice compared to the vehicle control that is likely due to the PSCA downregulation seen by *ex vivo* flow cytometry.

In summary, the majority of local prostate cancer tumors and metastases express PSCA and its expression correlates with tumor grade, stage, invasiveness, and metastatic potential. The A11 anti-PSCA minibody has shown the ability to specifically image PSCA expressing cells *in vivo* and has potential diagnostic utility in noninvasive imaging, staging, and risk stratification of prostate cancer (32). In this work, the A11 minibody achieved higher sensitivity and specificity than ^{18}F-Fluoride bone scans for detecting osteoblastic intratibial xenografts which may allow for earlier clinical metastasis detection and improved patient risk stratification. Furthermore, we demonstrated that A11 minibody immunoPET showed decreased tumor uptake in response to androgen deprivation *in vivo*. The A11 minibody, therefore, has clinical potential for monitoring the response to androgen deprivation and the development of castration resistance. As the response to ADT and development of androgen independence can be quite heterogeneous between different tumors, determination of whether a subset of tumors fails to respond to treatment could potentially allow for targeted therapies (e.g. external beam radiation) to have a larger role in treating metastatic disease or for a more prompt transition to systemic chemotherapy. We have, therefore, begun investigation of ^{124}I-labeled anti-PSCA A11 minibody in the clinical setting.

Supplementary Material

Refer to Web version on PubMed Central for supplementary material.

Acknowledgment

We thank Waldemar Ladno, Darin Williams, Melissa McCracken, Dr. David Stout, and Dr. John David for technical assistance with these experiments.

Financial support: NIH Grants CA092131, CA016042, and T32GM008042, Department of Defense W81WXH-08-1-0442, Department of Energy DE-SC0001220, and National Cancer Institute F30CA165824.

References

1. Schroder FH, Hugosson J, Roobol MJ, Tammela TL, Ciatto S, Nelen V, et al. Screening and prostate-cancer mortality in a randomized European study. N Engl J Med. 2009; 360:1320–1328. [PubMed: 19297566]
2. Siegel R, Naishadham D, Jemal A. Cancer statistics, 2013. CA Cancer J Clin. 2013; 63:11–30. [PubMed: 23335087]
3. Jadvar H. Molecular imaging of prostate cancer: PET radiotracers. AJR Am J Roentgenol. 2012; 199:278–291. [PubMed: 22826388]
4. Hricak H, Choyke PL, Eberhardt SC, Leibel SA, Scardino PT. Imaging Prostate Cancer: A Multidisciplinary Perspective. Radiology. 2007; 243:28–53. [PubMed: 17392247]
5. [cited 2014 June 1] ClinicalTrials.gov. [Internet]. F18PET/CT Versus TC-MDP Scanning to Detect Bone Mets. ClinicalTrials.gov registration number: NCT00882609.

6. Beheshti M, Vali R, Waldenberger P, Fitz F, Nader M, Loidl W, et al. Detection of bone metastases in patients with prostate cancer by 18F fluorocholine and 18F fluoride PET–CT: a comparative study. Eur J Nucl Med Mol Imaging. 2008; 35:1766–1774. [PubMed: 18465129]
7. Even-Sapir E, Metser U, Mishani E, Lievshitz G, Lerman H, Leibovitch I. The detection of bone metastases in patients with high-risk prostate cancer: 99mTc-MDP Planar bone scintigraphy, single- and multi-field-of-view SPECT, 18F-fluoride PET, 18F-fluoride PET/CT. J Nucl Med. 2006; 47:287–297. [PubMed: 16455635]
8. Grant FD, Fahey FH, Packard AB, Davis RT, Alavi A, Treves ST. Skeletal PET with 18F-Fluoride: Applying New Technology to an Old Tracer. J Nucl Med. 2007; 49:68–78. [PubMed: 18077529]
9. Harris WP, Mostaghel EA, Nelson PS, Montgomery B. Androgen deprivation therapy: progress in understanding mechanisms of resistance and optimizing androgen depletion. Nat Clin Pract Urol. 2009; 6:76–85. [PubMed: 19198621]
10. Scher HI, Beer TM, Higano CS, Anand A, Taplin ME, Efstathiou E, et al. Antitumour activity of MDV3100 in castration-resistant prostate cancer: a phase 1–2 study. Lancet. 2010; 375:1437–1446. [PubMed: 20398925]
11. Jung ME, Ouk S, Yoo D, Sawyers CL, Chen C, Tran C, et al. Structure-activity relationship for thiohydantoin androgen receptor antagonists for castration-resistant prostate cancer (CRPC). J. Med. Chem. 2010; 53:2779–2796. [PubMed: 20218717]
12. Tran C, Ouk S, Clegg NJ, Chen Y, Watson PA, Arora V, et al. Development of a second-generation antiandrogen for treatment of advanced prostate cancer. Science (New York, N.Y.). 2009; 324:787–790.
13. Evans MJ, Smith-Jones PM, Wongvipat J, Navarro V, Kim S, Bander NH, et al. Noninvasive measurement of androgen receptor signaling with a positron-emitting radiopharmaceutical that targets prostate-specific membrane antigen. Proc Natl Acad Sci U S A. 2011; 108:9578–9582. [PubMed: 21606347]
14. Scher HI, Fizazi K, Saad F, Taplin ME, Sternberg CN, Miller K, et al. Increased survival with enzalutamide in prostate cancer after chemotherapy. N Engl J Med. 2012; 367:1187–1197. [PubMed: 22894553]
15. Nadiminty N, Gao AC. Mechanisms of persistent activation of the androgen receptor in CRPC: recent advances and future perspectives. World J Urol. 2012
16. Chan SC, Li Y, Dehm SM. Androgen receptor splice variants activate androgen receptor target genes and support aberrant prostate cancer cell growth independent of canonical androgen receptor nuclear localization signal. J Biol Chem. 2012; 287:19736–19749. [PubMed: 22532567]
17. Sun S, Sprenger CCT, Vessella RL, Haugk K, Soriano K, Mostaghel EA, et al. Castration resistance in human prostate cancer is conferred by a frequently occurring androgen receptor splice variant. J Clin Invest. 2010; 120:2715–2730. [PubMed: 20644256]
18. Ananias HJK, Heuvel MC van den, Helfrich W, Jong IJ de. Expression of the gastrin-releasing peptide receptor, the prostate stem cell antigen and the prostate-specific membrane antigen in lymph node and bone metastases of prostate cancer. Prostate. 2009; 69:1101–1108. [PubMed: 19343734]
19. Lam JS, Yamashiro J, Shintaku IP, Vessella RL, Jenkins RB, Horvath S, et al. Prostate stem cell antigen is overexpressed in prostate cancer metastases. Clin Cancer Res. 2005; 11:2591–2596. [PubMed: 15814638]
20. Barbisan F, Mazzucchelli R, Santinelli A, Scarpelli M, Lopez-Beltran A, Cheng L, et al. Expression of prostate stem cell antigen in high-grade prostatic intraepithelial neoplasia and prostate cancer. Histopathology. 2010; 57:572–579. [PubMed: 20955382]
21. Zhigang Z, Wenlv S. Prostate stem cell antigen (PSCA) expression in human prostate cancer tissues: implications for prostate carcinogenesis and progression of prostate cancer. Jpn J Clin Oncol. 2004; 34:414–419. [PubMed: 15342669]
22. Gu Z, Thomas G, Yamashiro J, Shintaku IP, Dorey F, Raitano A, et al. Prostate stem cell antigen (PSCA) expression increases with high gleason score, advanced stage and bone metastasis in prostate cancer. Oncogene. 2000; 19:1288–1296. [PubMed: 10713670]

23. Han KR, Seligson DB, Liu X, Horvath S, Shintaku PI, Thomas GV, et al. Prostate stem cell antigen expression is associated with gleason score, seminal vesicle invasion and capsular invasion in prostate cancer. J Urol. 2004; 171:1117–1121. [PubMed: 14767283]
24. Reiter RE, Gu Z, Watabe T, Thomas G, Szigeti K, Davis E, et al. Prostate stem cell antigen: a cell surface marker overexpressed in prostate cancer. Proc Natl Acad Sci U S A. 1998; 95:1735–1740. [PubMed: 9465086]
25. Reiter RE, Sato I, Thomas G, Qian J, Gu Z, Watabe T, et al. Coamplification of prostate stem cell antigen (PSCA) and MYC in locally advanced prostate cancer. Genes Chromosomes Cancer. 2000; 27:95–103. [PubMed: 10564591]
26. Zhao Z, Zeng G, Ma W, Ou L, Liang Y. Peripheral blood reverse transcription PCR assay for prostate stem cell antigen correlates with androgen-independent progression in advanced prostate cancer. Int J Cancer. 2012; 131:902–910. [PubMed: 21952944]
27. Jain A, Lam A, Vivanco I, Carey MF, Reiter RE. Identification of an androgen-dependent enhancer within the prostate stem cell antigen gene. Molecular Endocrinology. 2002; 16:2323–2337. [PubMed: 12351697]
28. Dubey P, Wu H, Reiter RE, Witte ON. Alternative pathways to prostate carcinoma activate prostate stem cell antigen expression. Cancer Res. 2001; 61:3256–3261. [PubMed: 11309275]
29. Zhigang Z, Wenlu S. Flutamide reduced prostate cancer development and prostate stem cell antigen mRNA expression in high grade prostatic intraepithelial neoplasia. Int J Cancer. 2008; 122:864–870. [PubMed: 17957793]
30. Zhigang Z, Wenlu S. Complete androgen ablation suppresses prostate stem cell antigen (PSCA) mRNA expression in human prostate carcinoma. Prostate. 2005; 65:299–305. [PubMed: 16015594]
31. Knowles SM, Wu AM. Advances in immuno-positron emission tomography: antibodies for molecular imaging in oncology. J. Clin. Oncol. 2012; 30:3884–3892. [PubMed: 22987087]
32. Knowles SM, Zettlitz KA, Tavare R, Rochefort MM, Salazar FB, Stout DB, et al. Quantitative ImmunoPET of Prostate Cancer Xenografts with 89Zr- and 124I-Labeled Anti-PSCA A11 Minibody. J Nucl Med. 2014; 55:452–459. [PubMed: 24504052]
33. Lepin EJ, Leyton JV, Zhou Y, Olafsen T, Salazar FB, McCabe KE, et al. An affinity matured minibody for PET imaging of prostate stem cell antigen (PSCA)-expressing tumors. Eur J Nucl Med Mol Imaging. 2010; 37:1529–1538. [PubMed: 20354850]
34. Craft N, Chhor C, Tran C, Belldegrun A, DeKernion J, Witte ON, et al. Evidence for clonal outgrowth of androgen-independent prostate cancer cells from androgen-dependent tumors through a two-step process. Cancer Res. 1999; 59:5030–5036. [PubMed: 10519419]
35. Hsu WK, Virk MS, Feeley BT, Stout DB, Chatziioannou AF, Lieberman JR. Characterization of osteolytic, osteoblastic, and mixed lesions in a prostate cancer mouse model using 18F-FDG and 18F-fluoride PET/CT. J Nucl Med. 2008; 49:414–421. [PubMed: 18287261]
36. Lee Y, Schwarz E, Davies M, Jo M, Gates J, Wu J, et al. Differences in the cytokine profiles associated with prostate cancer cell induced osteoblastic and osteolytic lesions in bone. J. Orthop. Res. 2003; 21:62–72. [PubMed: 12507581]
37. Campbell JP, Merkel AR, Masood-Campbell SK, Elefteriou F, Sterling JA. Models of bone metastasis. Journal of visualized experiments : JoVE. 2012:e4260. [PubMed: 22972196]
38. Loening AM, Gambhir SS. AMIDE: a free software tool for multimodality medical image analysis. Mol Imaging. 2003; 2:131–137. [PubMed: 14649056]
39. Rosset A, Spadola L, Ratib O. OsiriX: an open-source software for navigating in multidimensional DICOM images. Journal of digital imaging. 2004; 17:205–216. [PubMed: 15534753]
40. Gu Z, Yamashiro J, Kono E, Reiter RE. Anti-prostate stem cell antigen monoclonal antibody 1G8 induces cell death in vitro and inhibits tumor growth in vivo via a Fc-independent mechanism. Cancer Res. 2005; 65:9495–9500. [PubMed: 16230414]
41. Pariente N, Morizono K, Virk MS, Petrigliano FA, Reiter RE, Lieberman JR, et al. A novel dual-targeted lentiviral vector leads to specific transduction of prostate cancer bone metastases in vivo after systemic administration. Mol. Ther. 2007; 15:1973–1981. [PubMed: 17653099]

42. Feeley BT, Gamradt SC, Hsu WK, Liu N, Krenek L, Robbins P, et al. Influence of BMPs on the formation of osteoblastic lesions in metastatic prostate cancer. J. Bone Miner. Res. 2005; 20:2189–2199. [PubMed: 16294272]
43. Whang PG, Schwarz EM, Gamradt SC, Dougall WC, Lieberman JR. The effects of RANK blockade and osteoclast depletion in a model of pure osteoblastic prostate cancer metastasis in bone. J. Orthop. Res. 2005; 23:1475–1483. [PubMed: 16005175]
44. Miwa S, Mizokami A, Keller ET, Taichman R, Zhang J, Namiki M. The bisphosphonate YM529 inhibits osteolytic and osteoblastic changes and CXCR-4-induced invasion in prostate cancer. Cancer Res. 2005; 65:8818–8825. [PubMed: 16204052]
45. Singh AS, Figg WD. In vivo models of prostate cancer metastasis to bone. J Urol. 2005; 174:820–826. [PubMed: 16093963]
46. Berger F, Lee YP, Loening AM, Chatziioannou A, Freedland SJ, Leahy R, et al. Whole-body skeletal imaging in mice utilizing microPET: optimization of reproducibility and applications in animal models of bone disease. Eur J Nucl Med Mol Imaging. 2002; 29:1225–1236. [PubMed: 12418463]
47. Ulmert D, Evans MJ, Holland JP, Rice SL, Wongvipat J, Pettersson K, et al. Imaging androgen receptor signaling with a radiotracer targeting free prostate-specific antigen. Cancer discovery. 2012; 2:320–327. [PubMed: 22576209]
48. Shah RB, Mehra R, Chinnaiyan AM, Shen R, Ghosh D, Zhou M, et al. Androgen-independent prostate cancer is a heterogeneous group of diseases: lessons from a rapid autopsy program. Cancer Res. 2004; 64:9209–9216. [PubMed: 15604294]
49. Thurber GM, Weissleder R. Quantitating antibody uptake in vivo: conditional dependence on antigen expression levels. Mol Imaging Biol. 2011; 13:623–632. [PubMed: 20809210]
50. Wilks MQ, Knowles SM, Wu AM, Huang SC. Improved Modeling of In Vivo Kinetics of Slowly Diffusing Radiotracers for Tumor Imaging. J Nucl Med. 2014

Translational Relevance

Clinical detection of prostate cancer metastases and monitoring of the response to androgen deprivation therapy remains inadequate. We have previously developed an engineered anti-PSCA antibody fragment with affinity and pharmacokinetics optimized for imaging, the A11 minibody, and demonstrated high-contrast quantitative immunoPET imaging of PSCA expression. In this work, we investigate the translational applications of A11 minibody immunoPET. We demonstrate detection of bone tumors with higher sensitivity and specificity than ^{18}F-Fluoride bone scans and that the A11 minibody can detect tumor response to androgen deprivation earlier than conventional imaging. These results may directly translate into improved clinical metastasis detection and the ability to non-invasively image the efficacy of androgen deprivation therapy and the development of castration resistant prostate cancer. We have recently begun a clinical trial to compare A11 minibody immunoPET to bone scans in men with known metastatic disease to investigate this translational potential.

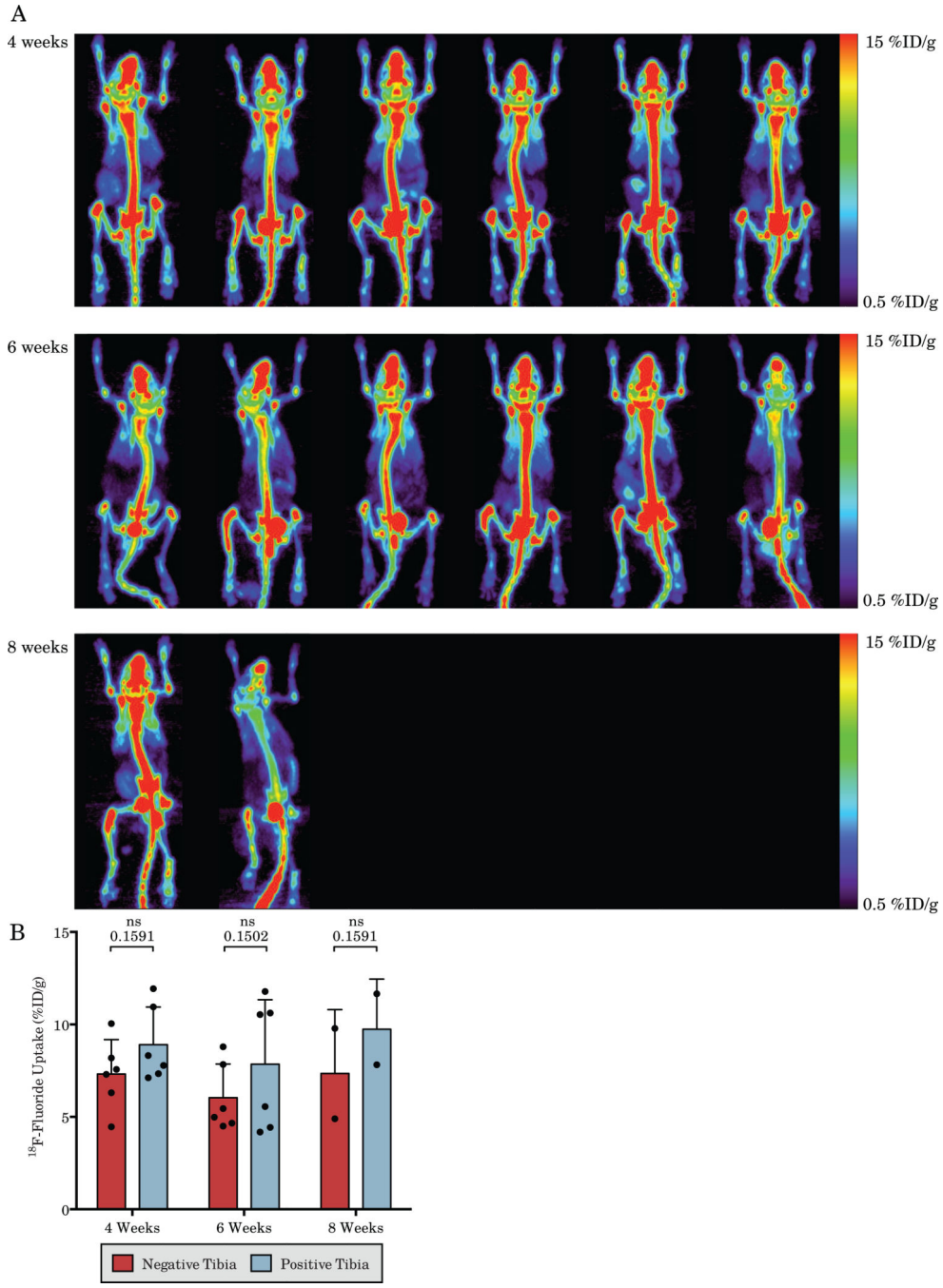

Figure 1.

Serial ^{18}F-Fluoride bone scans of mice bearing LAPC-9 intratibial xenografts (A) and quantification of the positive and negative tibias (B). Clear determination of increased signal in tumor bearing tibias is difficult due to the large degree of non-specific uptake. Each column displays serial imaging of the same mouse and each is matched with the corresponding A11 immunoPET in Figure 2.

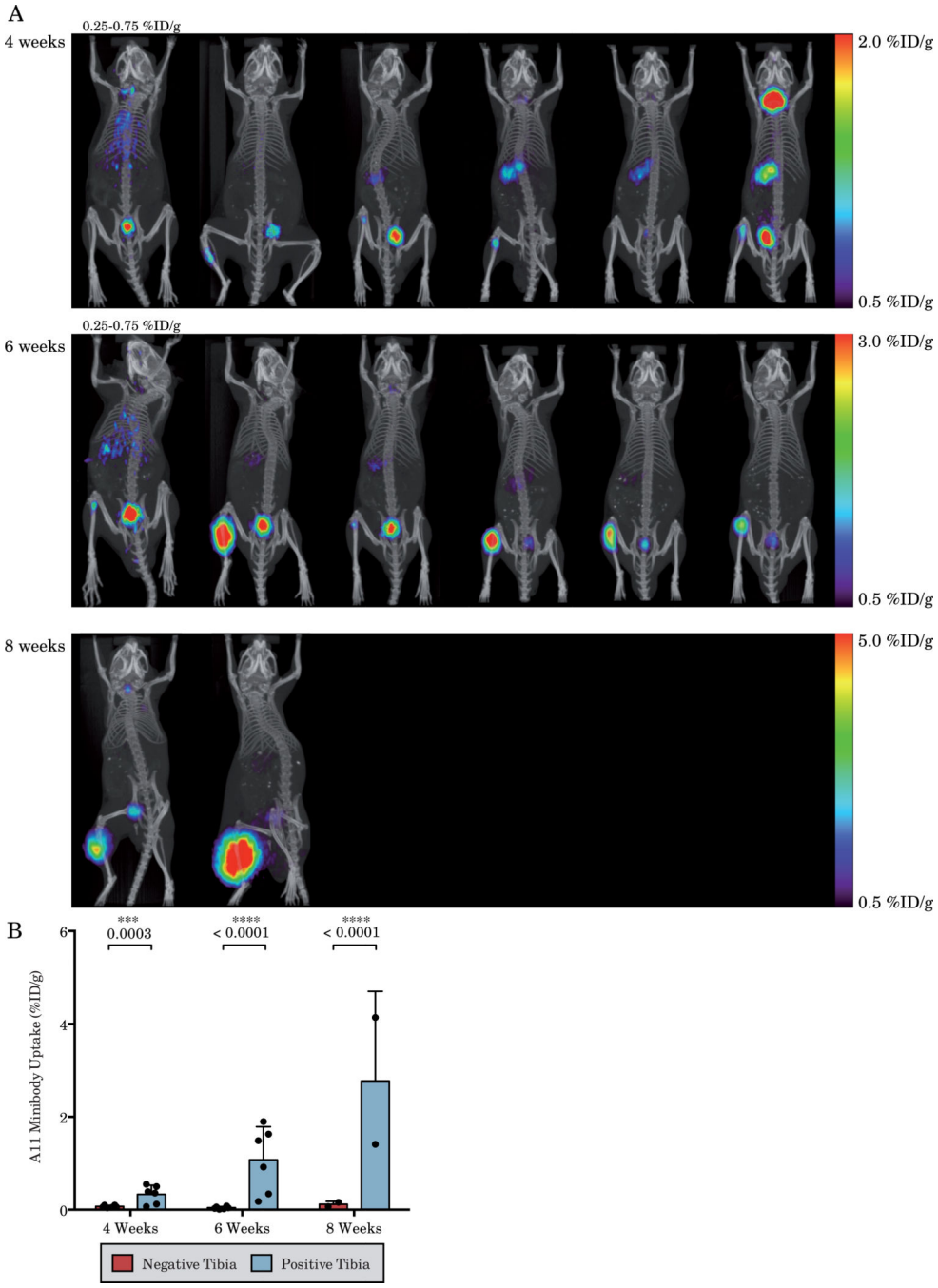

Figure 2.

Serial ^{124}I-anti-PSCA immunoPET imaging of mice bearing LAPC-9 intratibial xenografts (A) and quantification of the positive and negative tibias (B). Increased uptake of A11 minibody can be easily discerned in the majority of tumor bearing tibias. Each column displays serial imaging of the same mouse and each is matched with the corresponding ^{18}F-Fluoride bone scan in Figure 1. All mice are displayed on the scale indicated on the right except for those with a scale indicated directly above them.

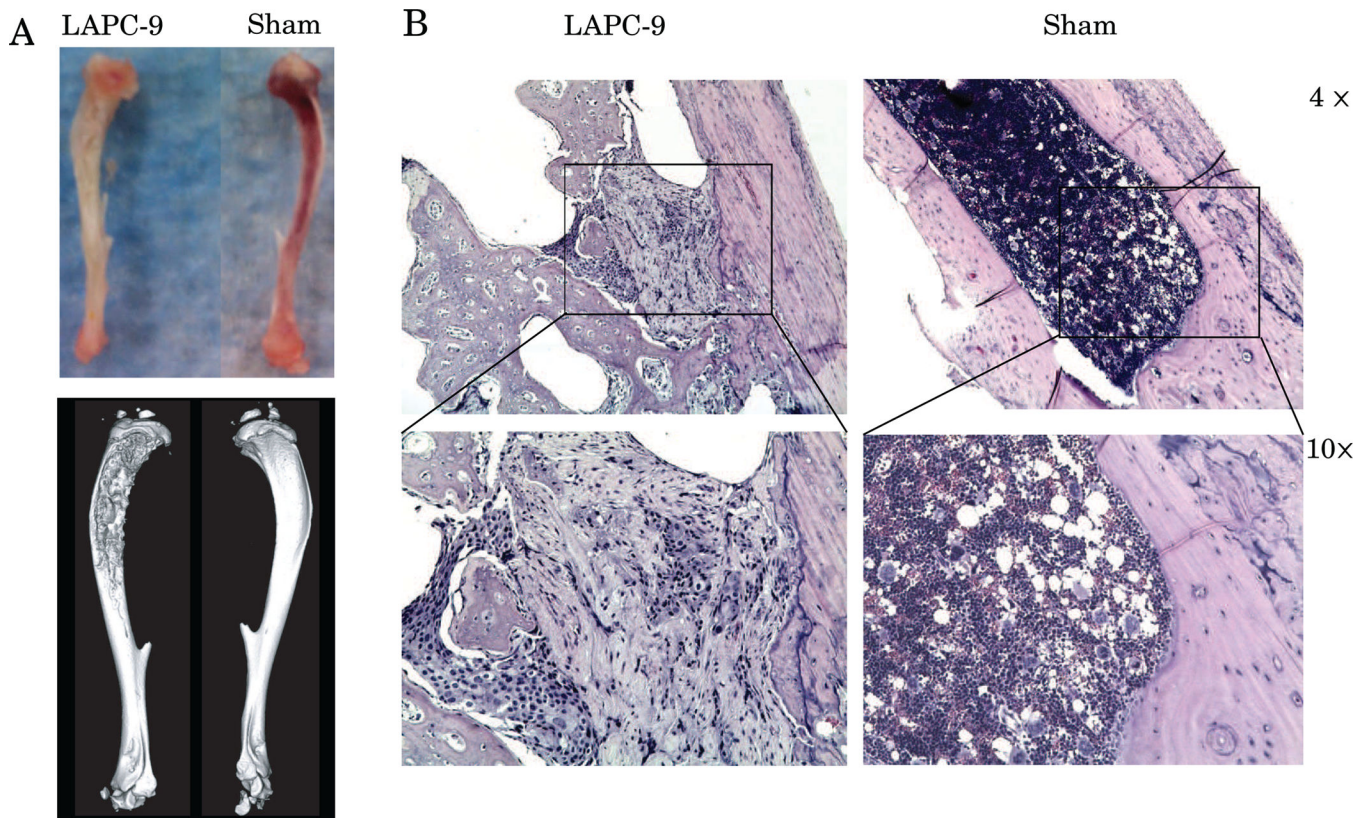

Figure 3.

At 6 weeks post-tumor inoculation, tibias bearing LAPC-9 intratibial xenografts grossly show bone marrow displacement by the tumor and high-resolution *ex vivo* microCT demonstrates osteoblastic changes in the LAPC-9 injected tibias with normal appearing sham controls (A). Histology of LAPC-9 bearing tibias shows tumor interspersed with osteoblastic bone formation whereas histology of sham tibias shows normal bone marrow (B).

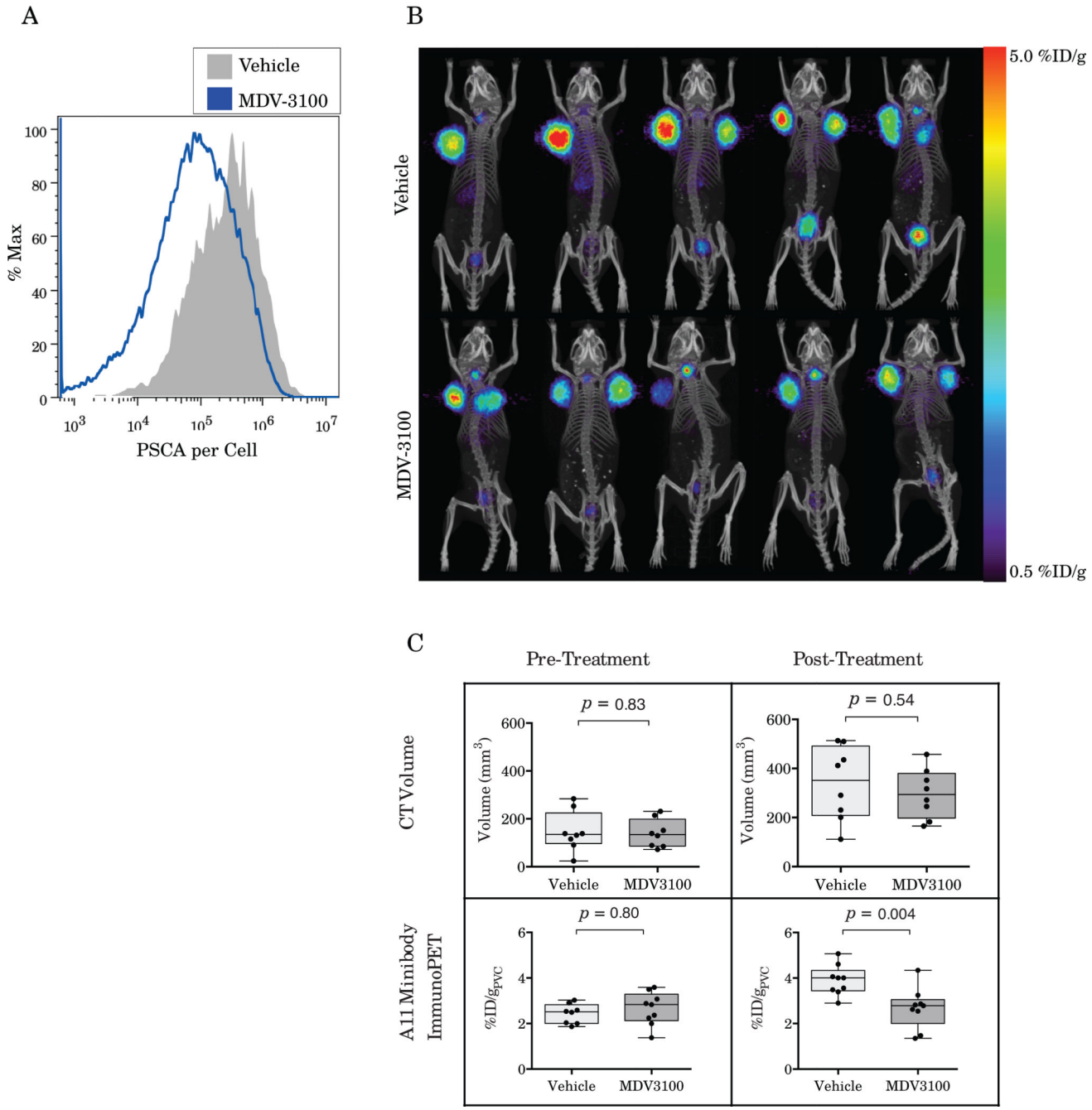

Figure 4.

Ex vivo quantitative flow cytometry shows downregulation of PSCA on LAPC-9 tumor cells in response to treatment with MDV-3100 (A). A11 minibody imaging of mice bearing LAPC-9 xenografts treated with MDV-3100 shows decreased tumor uptake *in vivo* as compared to vehicle controls (B). Quantification of the microPET/CT results shows no difference in tumor volumes or minibody uptake pre-treatment (C). However, following a week of treatment, A11 immunoPET shows significantly decreased uptake in MDV-3100

treated mice compared to vehicle controls (p=0.004) whereas CT volume shows no difference between the groups (p=0.54).

Table 1

44 hour biodistribution of ^{124}I-A11 minibody in mice bearing LAPC-9 intratibial xenografts at 6 and 8 weeks post-tumor implantation.

	LAPC-9 Intratibial Xenograft			
	6 weeks		8 weeks	
	n	%ID/g±SD	*n*	%ID/g±SD
Blood	4	0.57±0.15	2	0.45±0.11
Positive (Left) Tibia	4	1.51±0.79	2	1.50±0.35
Sham (Right) Tibia	4	0.08±0.03	2	0.12±0.00
Left Calf Muscle	4	0.45±0.33	2	2.54±1.26
Right Calf Muscle	4	0.06±0.02	2	0.07±0.01
Left Femur	4	0.10±0.03	2	0.14±0.03
Right Femur	4	0.10±0.03	2	0.13±0.00
Liver	4	0.14±0.02	2	0.28±0.04
Kidney	4	0.24±0.04	2	0.37±0.04
Spleen	3	0.18±0.08		
Heart	3	0.21±0.04		
Lung	3	0.32±0.07		
Carcass	4	0.12±0.04	2	0.25±0.05
Pos Tibia:Blood	4	2.85±1.49	2	3.55±1.68
Pos:Neg Tibia	4	18.98±7.10	2	12.50±2.98
Pos Tibia:Muscle	4	27.16±15.5	2	20.08±0.80

Table 2

Biodistribution of ^{124}I-A11 minibody in mice bearing LAPC-9 xenografts at 44 hours post-injection show decreased uptake in MDV-3100 (40mg/kg) treated mice compared to vehicle control.

	Vehicle		MDV-3100		
	n	**%ID/g±SD**	***n***	**%ID/g±SD**	***p***
LAPC-9	9	3.63±0.59	9	2.75±0.95	**0.03**
Blood	5	0.65±0.11	5	0.61±0.14	0.63
Liver	5	0.19±0.01	5	0.18±0.03	0.48
Kidney	5	0.26±0.03	5	0.26±0.08	0.95
Heart	5	0.32±0.06	5	0.25±0.05	0.08
Lungs	5	0.54±0.08	5	0.62±0.19	0.42
Spleen	5	0.27±0.04	5	0.36±0.11	0.15
Stomach	5	0.38±0.09	5	0.30±0.05	0.14
Tail	5	0.56±0.27	5	0.59±0.25	0.86
Muscle	5	0.05±0.02	5	0.05±0.01	0.92
Carcass	5	0.13±0.02	5	0.12±0.02	0.57
Tumor:Blood	9	5.58±1.07	9	4.51±1.32	0.08
Tumor:Muscle	9	74.0±29.1	9	53.6±17.7	0.09